

# A Temperature and Emissivity Separation Algorithm for Advanced Spaceborne Thermal Emission and Reflection Radiometer (ASTER) Images

Alan Gillespie, Shuichi Rokugawa, Tsuneo Matsunaga, J. Steven Cothorn, Simon Hook, and Anne B. Kahle

**Abstract**—The Advanced Spaceborne Thermal Emission and Reflection Radiometer (ASTER) scanner on NASA's Earth Observing System (EOS)-AM1 satellite (launch scheduled for 1998) will collect five bands of thermal infrared (TIR) data with a noise equivalent temperature difference ( $NE\Delta T$ ) of  $\leq 0.3$  K to estimate surface temperatures and emissivity spectra, especially over land, where emissivities are not known in advance. Temperature/emissivity separation (TES) is difficult because there are five measurements but six unknowns. Various approaches have been used to constrain the extra degree of freedom. ASTER's TES algorithm hybridizes three established algorithms, first estimating the normalized emissivities and then calculating emissivity band ratios. An empirical relationship predicts the minimum emissivity from the spectral contrast of the ratioed values, permitting recovery of the emissivity spectrum. TES uses an iterative approach to remove reflected sky irradiance. Based on numerical simulation, TES should be able to recover temperatures within about  $\pm 1.5$  K and emissivities within about  $\pm 0.015$ . Validation using airborne simulator images taken over playas and ponds in central Nevada demonstrates that, with proper atmospheric compensation, it is possible to meet the theoretical expectations. The main sources of uncertainty in the output temperature and emissivity images are the empirical relationship between emissivity values and spectral contrast, compensation for reflected sky irradiance, and ASTER's precision, calibration, and atmospheric compensation.

**Index Terms**—Algorithms, emission, image analysis, infrared imaging, remote sensing, temperature measurement.

## I. INTRODUCTION

LAND surface temperatures are important in global-change studies, in estimating radiation budgets, in heat-balance studies, and as control for climate models. Emissivities are strongly indicative, even diagnostic, of composition, especially for the silicate minerals that make up much of the land surface. Surface emissivities are thus important for studies of soil development and erosion and for estimating amounts and changes in sparse vegetative cover for which the substrate

is visible. They are also important for bedrock mapping and resource exploration.

A new algorithm for determining land-surface temperatures ( $T$ ) and emissivity ( $\epsilon$ ) spectra for multispectral thermal infrared (8–12  $\mu\text{m}$ ) images has been developed for use with data from the Advanced Spaceborne Thermal Emission and Reflection Radiometer (ASTER), scheduled to be launched in 1998 on the first of NASA's Earth Observing System polar-orbiting spacecraft EOS-AM1. This temperature and emissivity separation (TES) algorithm relies on an empirical relationship between spectral contrast and minimum emissivity, determined from laboratory and field emissivity spectra to equalize the number of unknowns and measurements so that the set of Planck equations for the measured thermal radiances can be inverted. TES is adaptable to multispectral images from imaging systems other than ASTER.

The key goals of TES are to 1) estimate accurate and precise surface temperatures, especially over vegetation, water, and snow and 2) recover accurate and precise emissivities for mineral substrates. The TES algorithm is designed to produce "seamless" images—in other words, there should be no artifactual discontinuities, such as can be introduced by classification. TES embodies the simplest approach feasible, consistent with the above goals.  $T$  (one band) and  $\epsilon$  (five bands) images will be available as standard products from EOS.

Thermal infrared (TIR) radiances vary with both  $T$  and  $\epsilon$ , which therefore must be recovered from the measurements. Surface temperatures are independent of wavelength and can be recovered from even a single band of radiance data, provided atmospheric characteristics can be specified and the surface emissivity is known. Except for water, vegetation, and snow or ice, however, the emissivity of the land surface is not known *a priori*, but must be determined along with the temperature. The inversion for  $T$  and  $\epsilon$  is therefore underdetermined; there is always at least one more unknown than the number of measurements. Separation of  $T$  and  $\epsilon$  data from the measured radiances thus requires additional information, determined independently. In the TES algorithm, the additional constraint comes from the regression of minimum emissivity to spectral contrast calculated from laboratory spectra. At least three or four spectral bands are required to measure the contrast in images. Therefore, it is necessary to make multispectral measurements to determine land surface temperatures. This is not the case for sea-surface temperature estimation, for

Manuscript received October 31, 1997; revised March 18, 1998. This work was supported by the NASA EOS Project and ERSDAC.

A. Gillespie and J. S. Cothorn are with the Department of Geological Sciences, University of Washington, Seattle, WA 98195-1310 USA (e-mail: alan@rad.geology.washington.edu).

S. Rokugawa is with the Faculty of Engineering, University of Tokyo, Bunkyo-ku, Tokyo, 113 Japan.

T. Matsunaga is with the Geological Survey of Japan, Tsukuba, Ibaraki, 305 Japan.

S. Hook and A. B. Kahle are with the Jet Propulsion Laboratory, California Institute of Technology, Pasadena, CA 91109 USA.

Publisher Item Identifier S 0196-2892(98)04808-6.

example, because the emissivity spectrum of water is well known *a priori*.

The minimum number of bands necessary to recover land surface temperatures may be too small for surface composition mapping; because emissivity spectra of geologic materials can be quite complex, many emissivity studies require as many spectral bands in the TIR window as possible. Current engineering limitations prevent TIR imaging spectroscopy from satellite, and multispectral sensors with a handful of spectral bands are a compromise.

This paper presents the TES algorithm, results of a validation experiment, and TES  $T$  and  $\epsilon$  images calculated from six-band airborne Thermal Infrared Multispectral Scanner (TIMS) images [1] processed to simulate ASTER data. Discussion focuses on the theoretically predicted and experimentally determined precision and accuracy estimates as well as on the fundamental factors limiting TES performance.

## II. ASTER IMAGING SYSTEM

ASTER includes a five-band multispectral TIR scanner designed for recovery of land-surface "kinetic" temperatures and emissivities, not just temperatures over homogeneous surfaces of known emissivity, such as water. It is designed to obtain a global emissivity map of the land surface, but it will also recover surface temperatures and emissivities for requested localities for the entire six-year lifetime of EOS-AM1. With a TIR spatial resolution of 90 m and a VNIR resolution of 15 m, ASTER acts as a high-resolution complement to other EOS imaging experiments. Because of their high resolution, ASTER  $T$  and  $\epsilon$  data can be verified by field experiments and, at the same time, be used to understand the averaged responses of the lower resolution scanners.

ASTER has three bands in the visible and near-infrared (VNIR) spectral range (0.5–0.9  $\mu\text{m}$ ) with 15-m spatial resolution, six in the shortwave infrared (SWIR: 1.6–2.4  $\mu\text{m}$ ) with 30-m resolution, and five in the thermal infrared (TIR: 8–12  $\mu\text{m}$ ), with 90-m resolution [2], [3]. These 14 bands are collected in three down-looking telescopes that may be slewed  $\pm 8.5^\circ$  (SWIR, TIR) or  $\pm 24^\circ$  (VNIR) in the cross-track direction. Combined with the field-of-view (FOV) of  $\pm 2.5^\circ$ , the maximum TIR view angle is thus  $11^\circ$ . An additional backward-viewing telescope with a single band duplicating VNIR band 3 will provide the capability for same-orbit stereogrammetric data. The five TIR bands (ASTER bands 10–14) have spectral ranges of 8.125–8.475, 8.475–8.825, 8.925–9.275, 10.25–10.95, and 10.95–11.65  $\mu\text{m}$ , respectively. ASTER's estimated TIR radiometric accuracy at 300 K is 1 K; at 240 K it is 3 K. Radiometric precision (noise equivalent temperature difference or  $NE\Delta T$ ) at 300 K is  $\leq 0.3$  K [4].

The ASTER team located all five TIR bands within the 8–14- $\mu\text{m}$  atmospheric window to maximize geologic information. Because no spectral bands are located at the edges of the window, where atmospheric water absorbs ground emittance, it is not possible to estimate atmospheric profiles and parameters directly from ASTER images. The ASTER instrument team does compensate all measurements for atmospheric transmis-

sivity and path radiance and reports values for downwelling sky irradiance, all determined independently from other EOS data [5], so it is, in principle, possible to calculate accurate values of  $T$  and  $\epsilon$ . Nevertheless, actual ASTER  $T$  and  $\epsilon$  data may have complex patterns of inaccuracies because neither the atmospheric sounding nor the Moderate Resolution Imaging Spectroradiometer (MODIS) atmospheric profiles [6] available from the EOS-AM1 platform are at the 90-m scale of the ASTER TIR images.

The ASTER instrument is being provided by the Japanese Government under the Ministry of International Trade and Industry (MITI). The ASTER project is implemented through the Earth Remote Sensing Data Analysis Center (ERSDAC), Tokyo, Japan, and the Japan Resources Observation System Organization (JAROS), Tokyo, a nonprofit organizations under MITI. JAROS is responsible for the design and development of the ASTER instrument, which will be built by the Nippon Electric Company (NEC), Yokohama, Japan, the Mitsubishi Electric Corporation (MELCO), Kamakura, Japan, Fujitsu, Tokyo, Japan, and Hitachi, Tokyo, Japan.

## III. BACKGROUND

A surface radiates energy in proportion to its temperature ( $T$ ) and emissivity ( $\epsilon$ ). On the earth, atmospheric opacity restricts the TIR measured by spacecraft to spectral windows at wavelengths of 3–5 and 8–14  $\mu\text{m}$ . ASTER bands 10–14 lie within the TIR window of 8–14  $\mu\text{m}$ . The basic problem in estimating  $T$  and  $\epsilon$  is that the data are nondeterministic; there are more unknowns than measurements because there is an  $\epsilon$  for each image band, plus  $T$  and atmospheric parameters. This is the case even if the scene is isothermal and consists of a single material of uniform texture and topographic slope and aspect. Consequently, even if atmospheric parameters are measured independently, at least one additional degree of freedom must be constrained independently of ASTER. There are several ways to constrain the extra degrees of freedom, resulting in a variety of approaches and algorithms to  $T$  and  $\epsilon$  separation. Below, the important equations governing TIR remote sensing and previous solutions are reviewed. The TES algorithm is then introduced and its performance is evaluated.

### A. Conceptual Framework for TIR Remote Sensing

Temperature is not an intrinsic property of the surface: it varies with the irradiance history and meteorological conditions. Emissivity is an intrinsic property of the surface and is independent of irradiance. The radiance from a perfect emitter (i.e., a blackbody for which  $\epsilon = 1$ ) increases, approximately exponentially, with temperature, as described by Planck's Law. The radiance  $R$  emitted from a real surface, however, is less by the factor  $\epsilon$ :  $R_\lambda = \epsilon_\lambda B_\lambda$ , where  $B$  is the blackbody radiance and  $\lambda$  is wavelength ( $\mu\text{m}$ ). Within its 90-m pixels, ASTER integrates radiance emitted from a number of surface elements, potentially having different temperatures and compositions. The emitted radiance is attenuated during passage through the atmosphere, which also emits TIR radiation. Some of this radiance is emitted directly into the scanner ("path radiance")

some strik  
for most, I  
local zenith  
law:  $\rho_\lambda =$   
radiance  $L$

$L_\lambda, \mu, \lambda = \tau$

where

$x, y$  po  
do  
 $\pi$   
inc  
ele  
atr  
up  
(V

It has  
an, emit  
ough thi  
quantit  
assumptio  
an angl  
ther ima  
the edg  
may be er  
assumptio  
images fr  
For mo  
surfaces v  
Radiance  
order of 1  
typical or  
estimated  
re  $\tau \approx$   
the effec  
ground-er  
necessary  
reflected

accurately  
pixels) v  
than  $S_1$  a  
problem 1  
mores th  
does 7  
Equatic  
length an  
surfaces.  
of wavel  
small. At  
rial surfa  
emissivity  
compone

some strikes the ground and is then reflected into the scanner. For most, perhaps all, terrestrial surfaces viewed from near the local zenith, the reflectivity  $\rho$  and  $\varepsilon$  are related by Kirchhoff's Law:  $\rho_\lambda = 1 - \varepsilon_\lambda$ . A simplified expression for the measured radiance  $L$  is

$$L_{x,y,\lambda} = \tau_{x,y,\lambda} \left( \varepsilon_{x,y,\lambda} B_\lambda(T_{x,y}) + \rho_{x,y,\lambda} \left( S_{\downarrow x,y,\lambda} + \frac{1}{\pi} \sum_{m=-\infty}^{\infty} \sum_{n=-\infty}^{\infty} R_{x+m,y+n,\lambda}^* \right) \right) + S_{\uparrow x,y,\lambda} \quad (1)$$

where

- $x, y$  position in scene ( $m$ );
- $S_{\downarrow}$  downwelling atmospheric irradiance, normalized by  $\pi$  sr ( $\text{Wm}^{-2} \mu\text{m}^{-1} \text{sr}^{-1}$ );
- $R^*$  incident radiance emitted from adjacent scene elements ( $\text{Wm}^{-2} \mu\text{m}^{-1}$ );
- $\tau$  atmospheric transmissivity (dimensionless);
- $S_{\uparrow}$  upwelling atmospheric path radiance ( $\text{Wm}^{-2} \mu\text{m}^{-1} \text{sr}^{-1}$ ).

It has been assumed that the land surface is Lambertian, emitting TIR radiance equally in all directions, even though this assumption is not strictly necessary to solve (1) or quantitatively interpret the ASTER emissivity data. This assumption appears to be valid for the restricted range of scan angles planned for ASTER ( $\leq 11^\circ$ ), but may not be for other imaging systems with wider FOV's. Even for ASTER, at the edges of the images exitance angles of as much as  $50^\circ$  may be encountered locally on steep slopes. To the extent the assumption is violated, it will be difficult to relate ASTER  $\varepsilon$  images from data taken at different viewing angles.

For most terrestrial surfaces,  $0.7 < \varepsilon < 1.0$ , although surfaces with  $\varepsilon < 0.85$  are probably restricted to deserts [7]. Radiance emitted at  $10 \mu\text{m}$  from a surface at 300 K is on the order of  $10 \text{ Wm}^{-2} \mu\text{m}^{-1} \text{sr}^{-1}$ . For a sea-level summer scene, typical order-of-magnitude values of the atmospheric variables estimated by the MODTRAN3 atmospheric model [8]–[10] are  $\tau \approx 70\%$ ,  $S_{\uparrow} \approx 2.4$ , and  $S_{\downarrow} \approx 3.7 \text{ Wm}^{-2} \mu\text{m}^{-1} \text{sr}^{-1}$ . One effect of  $S_{\downarrow}$  is to reduce the spectral contrast of the ground-emitted radiance because of Kirchhoff's Law. It is necessary to compensate for atmospheric effects, including  $S_{\downarrow}$  reflected from the ground, if  $T$  and  $\varepsilon_\lambda$  are to be recovered accurately. Incident radiance from adjacent scene elements (pixels) varies with terrain roughness, but it is typically less than  $S_{\downarrow}$  and is usually ignored. Therefore, the remote-sensing problem reduces to  $L \approx \tau \varepsilon B(T) + \tau \rho S_{\downarrow} + S_{\uparrow}$ . Equation (1) ignores the effects of the atmospheric point spread function, as does TES.

Equation (1) describes only the radiance at a single wavelength and only the radiance from homogeneous isothermal surfaces. In practice, the radiance is measured over a band of wavelengths; however, errors due to this integration are small. At the 90-m scale of ASTER TIR pixels, many terrestrial surfaces consist of multiple components having different emissivity spectra and temperatures. Strictly speaking, each component adds to the number of unknowns, while the number

of measurements is unchanged. ASTER TIR measurements for such complex surfaces are not sufficient to estimate all of the unknowns; instead, it is necessary to determine only an effective  $T$  and  $\varepsilon$  spectrum for each pixel.

## B. Previous Approaches

Inversion of the TIR equations for  $T$  and  $\varepsilon$  have been attempted using deterministic and nondeterministic approaches. The former are restricted to areas for which one or more of the unknowns can be specified. Historically, the chief reason for TIR measurements has been to estimate temperatures. This task is deterministic for important scene types for which  $\varepsilon$  is not in question: the ocean [11], snowfields and glaciers, and closed-canopy forests. However, deterministic solutions require that the atmospheric parameters in (1) be measured directly and the measured radiance corrected for them, and this is not always feasible. Most ocean-temperature studies have utilized data from the Advanced Very High Resolution Radiometer (AVHRR), which has two TIR bands (4 and 5) at  $10.3\text{--}11.3 \mu\text{m}$  and  $11.5\text{--}12.5 \mu\text{m}$ , respectively, thereby "splitting" the TIR spectral window. Joint analysis of the two "split-window" bands can compensate for atmospheric effects while solving for  $T$  [12]–[14]. Split-window algorithms rely on empirical regression relating surface radiance measurements to water temperatures. A version of the split-window algorithm has been developed for EOS/MODIS images [15], [16].

Several authors have examined extending the "split-window" technique to land surfaces [17]–[19]. However, mixed results may be obtained over unvegetated surfaces due to unknown emissivity differences between bands. Inaccuracy of  $< 0.001$  in  $\varepsilon$  between AVHRR bands 4 and 5, for example, can lead to errors in  $T$  of 0.5 K [17], [18], [20]. In general, land emissivities cannot be estimated this closely and must be measured if accurate kinetic temperatures are to be recovered. As a result, the usefulness of split-window methods for land is limited to areas for which the emissivities are known *a priori*; elsewhere the nondeterministic nature of TIR remote sensing must be addressed head-on. Many geologic studies, however, have utilized enhancements such as decorrelation stretching that do not recover  $T$  and  $\varepsilon$  [21], [22]. A spectral-unmixing approach has been used to separate a nonlinear measure of  $T$  from  $\varepsilon$ , but the separation is imperfect [23].

In all, we examined 14 inversion methods for the general land-surface problem in creating TES [24]. These algorithms determine spectral shape but not  $T$ , require multiple observations under different conditions, assume a value for one of the unknowns, assume a spectral shape, or assume a relationship between spectral contrast and  $\varepsilon$ . All require independent atmospheric correction. The temperature-independent spectral indexes (TISI) [25], thermal log residuals and alpha residuals [26], and spectral emissivity ratios [27], [28] all recover spectral shape and therefore require modification for the purposes of TES, which requires recovery of spectral amplitude and temperature as well as shape. The day-night method [29] measures the same scene in two or more bands at different times, thereby increasing the number of unknowns by one (the second temperature; the emissivity is unchanged) but doubling the number of measurements, making the problem

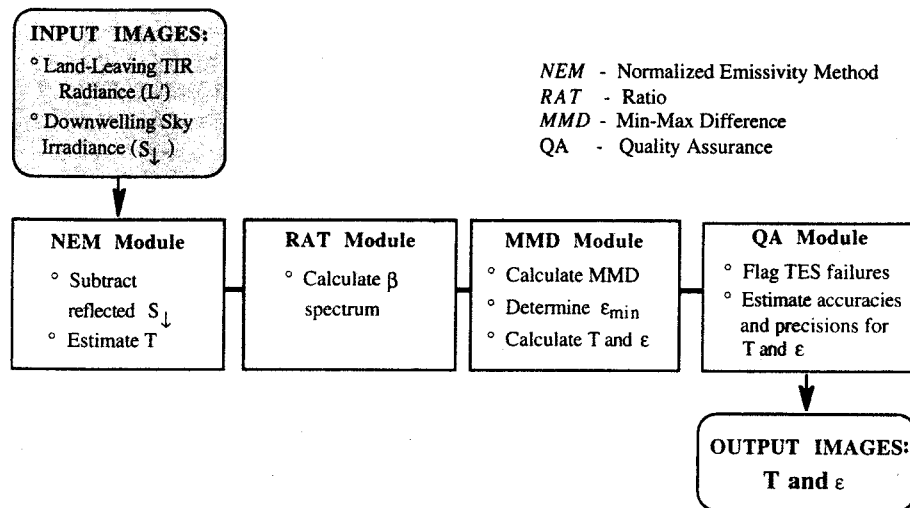


Fig. 1. Basic design of the TES algorithm.

overdetermined. In practice, however, this approach magnifies measurement "noise" and requires highly accurate ( $\ll 1$  pixel) registration between the two images. Other techniques have been based on an assumed value for a "model" emissivity at one wavelength [30], or an assumed maximum emissivity value at an unspecified wavelength (normalized emissivity method: NEM) [31], [32]. These approaches are unsatisfactory for ASTER because inaccuracies tend to be high ( $\pm 3$  K) and tilts are introduced into the  $\epsilon$  spectra by errors in the assumed emissivity value. Finally, the "alpha-derived emissivity" (ADE) method utilizes an empirical relationship between the standard deviation and mean emissivity to restore amplitude to the alpha-residual spectrum, thereby recovering  $T$  also [26], [33], [34]. The alpha-residual method relies on Wien's approximation ( $\exp(x) - 1 \approx \exp(x)$ ), takes the logarithm of both sides of the simplified (1), and then takes the difference of the terms for each band and the band-average to relate  $\epsilon$  to  $R$ , independent of  $T$ . In both the alpha-residual and ADE methods, however, the use of Wien's approximation introduces slope errors into the  $\epsilon$  spectrum, detectable by ASTER. The Mean-MMD method is based on a regression of laboratory emissivity values onto the maximum-minimum apparent emissivity difference (MMD), similar to and derived from the ADE approach. The apparent emissivities may be calculated by the model emissivity or NEM's. The MMD is converted to a mean emissivity by means of the regression, and the individual recovered emissivities may be rescaled accordingly. The Mean-MMD method avoids Wien's approximation and therefore has lesser slope errors in the recovered emissivities than the ADE spectra [35].

The instrument team for EOS/MODIS has developed a sophisticated approach to TES that is adaptable to scene circumstances; one path is the day-night approach, and in another, emissivities are specified by classifying VNIR/SWIR data [36], [37]. Although important scene types, such as vegetation, are readily identified in the VNIR and have well-known  $\epsilon$  spectra, thereby eliminating the indeterminacy, classification is ineffective for many geological materials. It also creates sharp boundaries in images of gradual transitions.

#### IV. TES ALGORITHM

The TES algorithm combines attractive features of three precursors and some new features (Fig. 1). It is most closely related to the Mean-MMD method. Essentially, TES uses the NEM algorithm to estimate  $T$ , from which emissivities are estimated and ratioed to their mean, producing  $\beta$  values. The  $\beta$  spectrum preserves the shape, but not the amplitude, of the actual emissivities. To recover the amplitude and, hence, a refined estimate of the temperature, the MMD is calculated and used to predict the minimum emissivity ( $\epsilon_{\min}$ ). TES operates on ASTER "land-leaving" TIR radiance data ( $L$ ), which have already been corrected for atmospheric  $\tau$  and  $S_{\downarrow}$  [5]. The same ASTER standard product also reports  $S_{\downarrow}$ , which cannot be removed without knowledge of  $\epsilon$ . TES removes reflected  $S_{\downarrow}$  iteratively [38]. TES also differs from precursors in the following ways:

- 1) refining the value of the maximum local emissivity  $\epsilon_{\max}$  used in the NEM, pixel by pixel;
- 2) correcting inaccuracies in  $\epsilon_{\min}$  for graybodies (e.g., vegetation) caused by errors in MMD due to  $NE\Delta T$ ;
- 3) using the first-generation TES  $T$  and  $\epsilon$  values to refine the correction for  $S_{\downarrow}$ , leading to more accurate second-generation estimates.

Finally, TES estimates and reports pixel-by-pixel accuracies and precisions for  $T$  and  $\epsilon$  in a "quality assurance" or QA data plane that is part of the ASTER standard product (see below). Presentation of TES herein is necessarily brief; more complete documentation is available from NASA [24]. In Fig. 1 and the subsequent discussion, the TES code is subdivided into modules named for the algorithms from which they are derived. The significant advance of the TES algorithm is to produce, for the first time, unbiased and precise estimates of emissivities and, therefore, improved estimates of surface temperatures for the land surface.

Numerical modeling suggests that, for most scenes, the TES algorithm can recover temperatures to within  $\sim 1.5$  K, assuming accurate radiometric measurements. Emissivities can

2. Fl  
minally c  
nk. Div i  
the nomina  
measur  
calculating

to recove  
and sea  
less ac  
surfa  
of magn  
data acqu  
Major li  
main sou  
bility of  
and spec  
factors.  
TES err

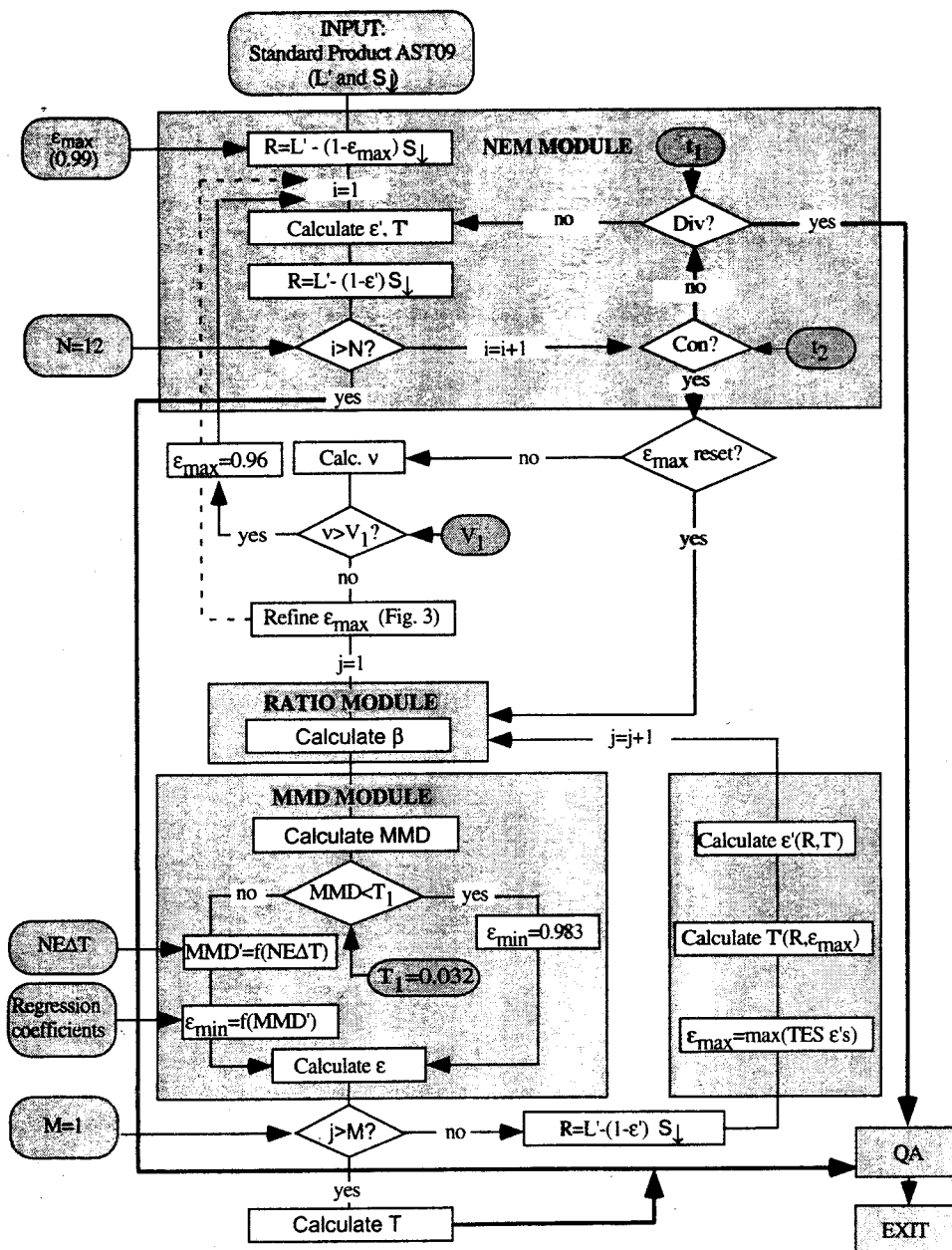


Fig. 2. Flow diagram of the TES algorithm, simplified in places.  $L' = \varepsilon B(T) + \rho S_1$  (i.e.,  $L' = R + \rho S_1$ ).  $R'$  here is the estimated surface-emitted radiance, nominally corrected for  $S_1$ ;  $R$  is the final corrected value. Tests for divergence (Div) and convergence (Con) determine if the correction for reflected  $S_1$  will work. Div is  $|\Delta^2 R / \Delta i^2| > t_1$ ; Con is  $|\Delta R / \Delta i| < t_2$  ( $\Delta R / \Delta i = R'_{i+1} - R'_i$ ). Parameters  $t_1$  and  $t_2$  are settable threshold values;  $i$  is the iteration number. The nominal value for  $\varepsilon_{\max}$  in the NEM module is refined if the spectral variance is small. The value for  $\varepsilon_{\min}$  found in the MMD module is compensated for measurement error. Finally, the TES  $\varepsilon$  data are used to refine  $R$  and the NEM  $T$ . Quality Assurance (QA) is specific to the ASTER project and consists of calculating TES performance and product characteristics and encoding them in a reserved data plane. Details of the of  $\varepsilon_{\max}$  refinement are shown in Fig. 3.

be recovered to within  $\sim 0.015$ . TES's performance over land and sea are comparable. ASTER TES temperature recovery is less accurate than the MODIS split-window algorithm for sea surfaces because ASTER resolution is better by an order of magnitude and its SNR is accordingly lower. ASTER's data acquisition plan, however, is focused on the land surface. Major limitations on algorithm performance arise from two main sources, in addition to sensor performance: 1) the reliability of the empirical relationship between emissivity values and spectral contrast and 2) the compensation for atmospheric factors. Measurement accuracy and precision contribute to TES errors but, individually at least, to a lesser degree.

TES accuracies and precisions are of the same size, but arise from different sources. Inaccuracies are due mainly to errors in atmospheric compensation, which are probably largely systematic; imprecision arises mainly from scatter in the  $\varepsilon_{\min}$ -MMD regression. Systematic errors across all five ASTER bands affect  $T$  directly, but random errors (or systematic errors that are focused in a single band) affect apparent spectral contrast and, therefore,  $\varepsilon$ . The  $\varepsilon_{\min}$ -MMD regression partly buffers  $\varepsilon$  against pan-ASTER radiometric and atmospheric inaccuracies because the amplitude is supplied from independent data. Instead, radiometric inaccuracies tilt the apparent  $\varepsilon$  spectrum, as does Wien's approximation.

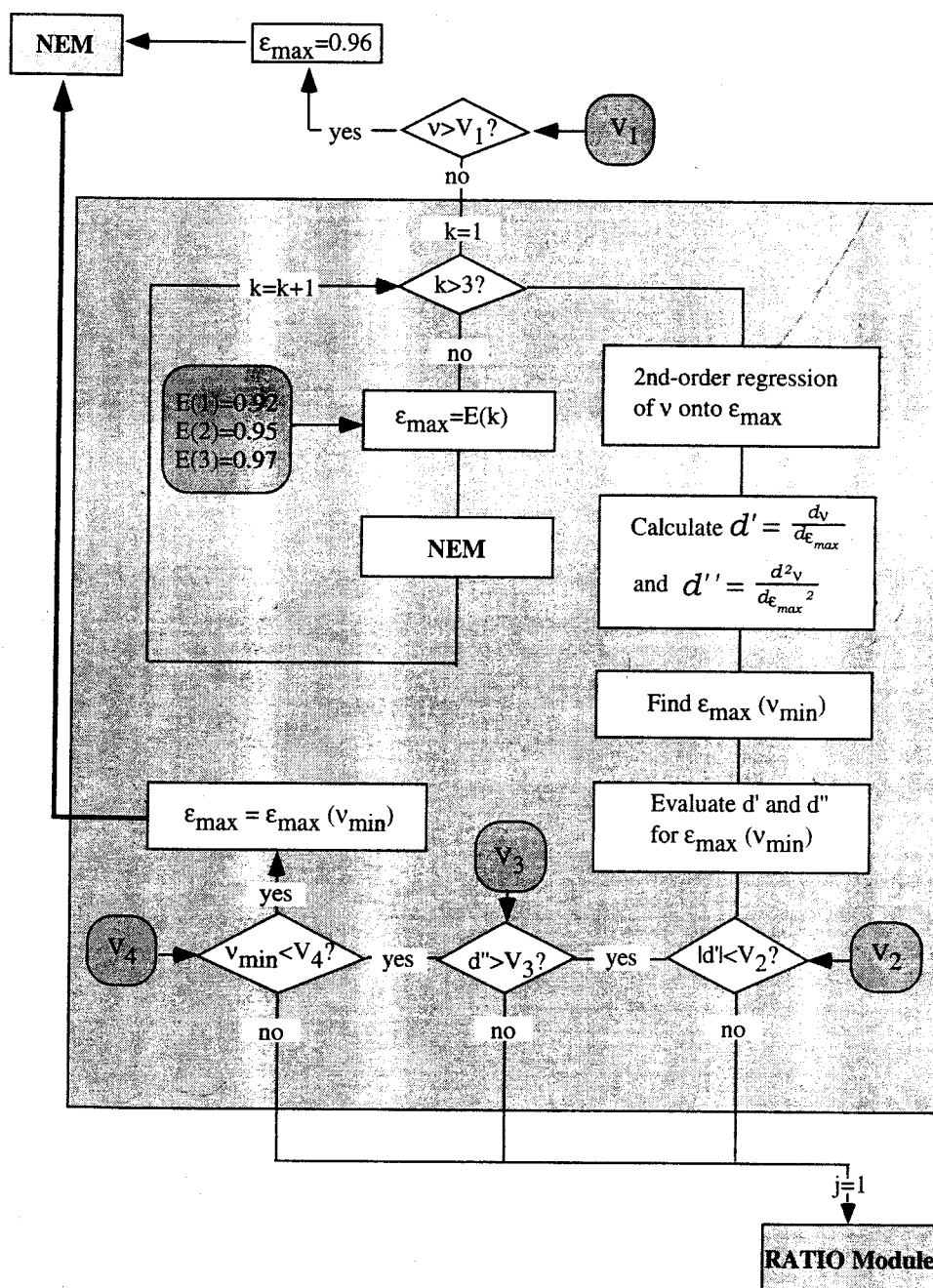


Fig. 3. Flow diagram of the part of the TES algorithm in which  $\epsilon_{\max}$  is refined (Fig. 2).

### B. Theoretical Basis for the TES Algorithm

Figs. 2 and 3 are flow diagrams of the TES algorithm. Below, the steps of the TES algorithm are presented in sufficient detail to permit regeneration of the processing code. The input ASTER image data sets consist of "land-leaving TIR radiance,"  $L'$ , and sky irradiance  $S_1$ , together comprising an ASTER standard product (AST09) [5].  $L'$  differs from the radiance measured at the spacecraft  $L$  (1) in that it has been compensated for atmospheric absorption and path radiance. These calibrated data have also been compensated for ASTER filter transmissivities and other instrument effects. Several TES parameters may be adjusted from their default values as the need arises. These parameters are identified in Fig. 1

and below. The output data sets consist of the five emissivity images (AST05), corresponding to ASTER bands 10–14 and a single image of surface temperature  $T$  (AST08).

1) *Estimating the Surface Temperature and Subtracting Reflected Sky Irradiance (NEM Module)*: The kinetic or "thermodynamic" temperature is estimated using the normalized emissivity approach. Essentially, a value for the maximum local emissivity  $\epsilon_{\max}$  is assumed to calculate a temperature and the other emissivities. A value of 0.99, near the upper end of the emissivity range for water, snow, and vegetation, is assumed to start with. If the NEM estimates of  $\epsilon$  have low contrast, it is likely that the initial assumption is nearly correct and an empirically based process, described below, is used to refine  $\epsilon_{\max}$ . If the contrast is high, the surface is probably

Because  
0.7 <  
to inacc  
random  
of the  
ASTER



rock or soil, and a lower value of  $\varepsilon_{\max} = 0.96$ , characteristic for those materials, is assumed and processing is restarted. For rock and soil, this lower default value cannot be refined. For all materials in the ASTER spectral library,  $0.94 < \varepsilon_{\max} < 1.00$ . Therefore, the estimated kinetic temperatures should be within  $\pm 3$  K at 340 K, and within  $\pm 2$  K at 273 K.

Upon entry to the NEM module, ground-emitted radiance  $R$  is estimated  $R = L' - (1 - \varepsilon_{\max})$ . The NEM temperature,  $T_{\text{NEM}}$  in (2), is taken to be the maximum temperature  $T_b$  estimated from the radiances  $R_b$  for the different image bands  $b$  ( $b = 10-14$  for ASTER)

$$T_b = \frac{c_2}{\lambda_b} \left( \ln \left( \frac{c_1 \varepsilon_{\max}}{\pi R_b \lambda_b^5} + 1 \right) \right)^{-1}, \quad T_{\text{NEM}} = \max(T_b)$$

$$\varepsilon_b = \frac{R_b}{B_b(T_{\text{NEM}})} \quad (2)$$

where  $c_1$  and  $c_2$  are the constants from Planck's Law. Once  $T_b$  is known, NEM emissivities,  $\varepsilon_b$  in (2), are calculated and used iteratively to reestimate  $R$ . This process is repeated until the change in  $R$  between steps is less than a settable threshold value  $t_2$ , or until the number of iterations exceeds a limit  $N$  (Fig. 2). The current default value for  $t_2$  is the radiance equivalent to the  $NE\Delta T$  and  $N = 12$ . If the slope of  $R$  versus iteration increases (such that  $|\Delta^2 R / \Delta i^2|$ , where  $i$  is the iteration number, exceeds a different settable threshold value  $t_1$ ) correction is not possible. Execution of TES is aborted, and the NEM  $T$  and  $\varepsilon$  values are reported. Correction for  $S_1$  is typically  $< 1$  K, unless the sky is warmer than the ground or humidity is high. Correction has the effect of increasing contrast in the emissivity spectrum, with the lowest values of  $\varepsilon$  being reduced the most. It follows that error introduced during correction also depends on  $\varepsilon$ , such that it is possible to recover accurate temperatures from the high- $\varepsilon$  image band even if the rest of the spectrum is inaccurate.

For samples with low contrast,  $\varepsilon_{\max}$  may be refined to improve accuracy. For near-graybodies, measurement error is the dominant source of spectral variance: the best value for  $\varepsilon_{\max}$  minimizes the variance  $v$  of the NEM emissivities. Plotting  $v$  against  $\varepsilon_{\max}$  yields an upwards-opening parabola. A new value of  $\varepsilon_{\max}$  may be found by calculating  $v(\frac{1}{5} \sum \varepsilon_b)^{-2}$  for  $\varepsilon_{\max} = 0.92, 0.95$ , and  $0.97$ , in addition to  $0.99$ , and fitting a parabola to the data. If this curve,  $v(\frac{1}{5} \sum \varepsilon_b)^{-2}$  versus  $\varepsilon_{\max}$ , has a minimum for  $0.9 < \varepsilon_{\max} < 1.00$ , it indicates the best estimate of  $\varepsilon_{\max}$ . In this case, the NEM module is executed with this final estimate to find new NEM emissivities.

2) *Ratio Algorithm (RATIO Module)*: The relative emissivities  $\beta_b$  are found by ratioing the NEM emissivities (2) to their average

$$\beta_b = \varepsilon_b 5 \left[ \sum \varepsilon_b \right]^{-1}, \quad b = 10, 14. \quad (3)$$

Because emissivities themselves are generally restricted to  $0.7 < \varepsilon_b < 1.0$ ,  $0.75 < \beta_b < 1.32$ . The errors in  $\beta$  due to inaccuracy in the NEM  $T$  are systematic but less than the random errors due to  $NE\Delta T$  for  $240 < T < 340$  K. Warping of the  $\beta$  spectrum is below the threshold of detectability for ASTER data.

3) *Estimating TES Emissivities and Temperature (MMD Module)*: The  $\beta$  spectrum must next be scaled to actual emissivity values, and the surface temperature must be recalculated from these new emissivities and from the atmospherically corrected radiances. These TES  $T$  and  $\varepsilon$  values comprise the ASTER Standard Products. An empirical relationship predicting  $\varepsilon_{\min}$  from MMD is used to convert  $\beta_b$  to  $\varepsilon_b$ . We established this regression using laboratory reflectance and field emissivity spectra [39], as discussed below.

The first step in the MMD module is to find the spectral contrast

$$\text{MMD} = \max(\beta_b) - \min(\beta_b), \quad b = 10-14 \quad (4)$$

from which the minimum emissivity is predicted and used to calculate the TES emissivities

$$\varepsilon_{\min} = 0.994 - 0.687 * \text{MMD}^{0.737}, \quad \varepsilon_b = \beta_b \left( \frac{\varepsilon_{\min}}{\min(\beta_b)} \right)$$

$$b = 10-14. \quad (5)$$

Provided that the actual emissivity contrast in a scene element is much greater than the apparent contrast, due only to measurement error, MMD is an unbiased estimate. For graybodies, however, MMD is dominated by measurement error and is no longer unbiased. That is, as the true spectral contrast is reduced to zero, MMD is also reduced, but to a positive limit whose value depends on the  $NE\Delta T$ . It is possible to correct the apparent MMD *pro forma*, as specified by Monte Carlo simulations

$$\text{MMD}' = [\text{MMD}^2 - cNE\Delta\varepsilon^2]^{-1}, \quad c = 1.52 \quad (6)$$

where  $\text{MMD}'$  is the corrected contrast,  $NE\Delta\varepsilon = 0.0032$  is calculated from  $NE\Delta T = 0.3$  K at 300 K, and the coefficient  $c$  was determined empirically. Equation (6) improves the accuracy of TES for graybodies, but at the expense of precision. We have found that if  $\text{MMD} < 0.03$ , the loss of precision becomes unacceptable. Therefore, when this is the case,  $\text{MMD}'$  is not calculated and  $\varepsilon_{\min}$  is not found from (5), but instead is set to 0.983, a value appropriate for water and close to values for vegetation canopies (although higher than values for individual leaves), and processing continues.

This assignment of a model  $\varepsilon_{\min}$  value essentially is a kind of classification of the TIR data for graybodies ( $\varepsilon_{\min}$  is assigned a default, representative value) and rocks and soils with high spectral contrast (TES is allowed to work as designed). In performing this classification, the goal of seamless output data products is jeopardized; step discontinuities may be encountered in transition areas between, for example, forests and arid steppes. If this turns out to be true, it may be possible to minimize the impact by adjusting the coefficient  $c$  in (6).

Up to this point, we have calculated a temperature with the NEM module  $T_{\text{NEM}}$  and a TES emissivity spectrum.  $T_{\text{NEM}}$  is likely to be in error by up to  $\sim 3$  K because the assumed value of  $\varepsilon_{\max}$  may have been inaccurate, especially for rocks, and even after all of the efforts to refine the estimate. This inaccuracy can be reduced by recalculating  $T$ , this time from

the measured, atmospherically corrected radiances  $R$  and the maximum value of the TES emissivity spectrum

$$T = \frac{c_2}{\lambda_{b^*}} \left( \ln \left( \frac{\varepsilon_{b^*} c_1}{R_{b^*} \pi \lambda_{b^*}^5} + 1 \right) \right)^{-1} \quad (7)$$

where  $b^*$  is the ASTER band for which emissivity  $\varepsilon_b$  is maximum (and correction for  $S_1$  is minimal).

4) *Final Correction for Sky Irradiance and Bias in  $\beta$* : The TES  $\varepsilon$  values are more accurate than the NEM values that were used to estimate reflected  $S_1$ . Recalculation of reflected  $S_1$ , based on the TES  $\varepsilon$  spectrum, therefore, can improve the accuracy of the  $T$  and  $\varepsilon$  output products. The TES  $\varepsilon$  values are used to make a final, single (noniterative) correction to  $R$ , and then new estimates of NEM  $\varepsilon$  are derived and used to recalculate the  $\beta$  spectrum (3). The improved TES  $\varepsilon$  and  $T$  are then calculated as before. For a variety of simulated and real radiance measurements, the "refined" TES emissivities changed by as much as 0.01; therefore, this final correction is worth doing. Experience shows that there is little gain with iteration.

5) *QA*: The TES algorithm applied to ASTER data will report on its performance and on the accuracy and precision of its  $T$  and  $\varepsilon$  products. The report will take the form of a header record and a 3-byte data plane. QA data will include flags to report on the optional paths through TES, described above, and flags marking defective pixels. Of central interest, however, is the reliability of the TES  $T$  and  $\varepsilon$  data, as tested by numerical simulation and by algorithm execution on different images simulated from laboratory and field spectrometer data [39]. TES performance depends strongly on the ratio of  $S_1$  to  $L'$  or  $R$  and on MMD, indicators that can be assessed pixel-by-pixel during operation. This information, together with the results of the numerical simulations, will be used to assign each pixel to an accuracy and precision category, which is then reported in the QA data. There will be three categories, each of temperature accuracy and temperature precision within 1.0 K, 1.0–2.0 K, and >2.0 K. There will be equivalent categories for emissivity: within 0.01, 0.01–0.02, and >0.02. TES performance is affected by the proximity of clouds; for daytime data, this information will be estimated from a classification of ASTER, VNIR, and SWIR data and will be reported in the QA plane.

### C. Regression of $\varepsilon_{\min}$ onto MMD

The relationship between emissivity and spectral contrast was established by analysis of 86 laboratory TIR reflectance spectra [45], equivalent to emissivity by Kirchhoff's Law. The data were converted to ASTER five-band pseudospectra, and  $\varepsilon_{\min}$  was found for each sample. Radiances were estimated, scaling emissivities by blackbody radiances calculated for  $T = 300$  K, and  $\beta$  spectra and its MMD were calculated. The  $\varepsilon_{\min}$  data were then regressed to the MMD values. They are empirically related by a simple power law [Fig. 4; (5)]. The regression parameters are insensitive to temperature. Although the regression parameters are defined empirically, the relationship itself is reasonable and physically predictable if deviation from blackbody behavior is due to molecular

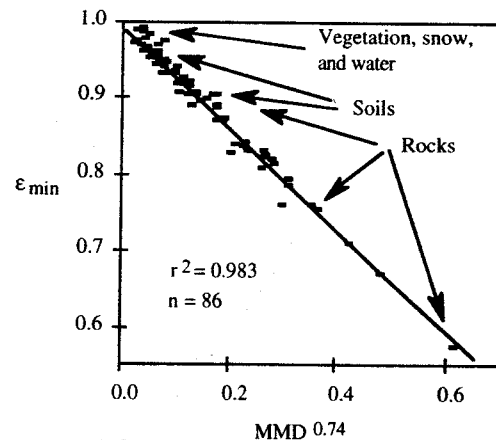


Fig. 4. Empirical relationship between  $\varepsilon_{\min}$  and MMD. The regression is based on 86 laboratory reflectance spectra of rocks, soils, vegetation, snow, and water, provided by [45]. Ninety-five percent of the samples fall within  $\pm 0.02$  emissivity units of the regression line. The  $\varepsilon_{\min}$ -MMD relationship follows a simple power law:  $\varepsilon_{\min} = 0.994 - 0.687 \text{ MMD}^{0.737}$  (parameter  $r^2$  is the regression coefficient;  $n$  is the number of samples).

resonance localized in narrow reststrahlen features. The regression chosen for the TES algorithm uses  $\varepsilon_{\min}$  rather than mean emissivity, as in the Mean-MMD algorithm, because it improved the correlation. The MMD was used because, for most spectra, it was just as good and faster to calculate than other measures of spectral complexity, such as variance.

The critical assumption that this regression applies to the entire gamut of surface materials has been tested and appears to be valid. A different set of 31 reflectance spectra [40], [41] yielded nearly identical regression coefficients [46], as did 145 field emissivity spectra of and playa and alluvial surfaces from Railroad Valley, NV [47], and 91 Australian rocks, all measured using the Jet Propulsion Laboratory's  $\mu\text{FTIR}$  spectrometer [39]. Finally, hundreds of airborne MIRACO<sub>2</sub>LAS CO<sub>2</sub> laser reflectance spectra, with a narrower window than the five ASTER TIR bands, yielded a regression having similar overall characteristics, but different coefficients [48].

Total scatter (95% or two standard deviations) about the regression line is about  $\pm 0.02$  emissivity units, equivalent to  $\pm 1.2$  K. This source of error in the ASTER temperature and emissivity products is intrinsic to the scene and cannot be reduced by increased measurement precision. Coincidentally, this is about the magnitude of imprecision, due to ASTER measurement error, evaluated by Monte Carlo techniques. It is also comparable to the predicted systematic inaccuracy of the ASTER TIR data of 1 K. The addition of one or two extra bands does not appear to greatly reduce the scatter: reduction of the number of bands to four likewise affects the imprecision little, depending on the choice of bands, but with further reduction to three it can increase greatly.

### D. Characterizing Atmospheric Effects

Compensating for atmospheric absorption and emittance relies on other instruments, especially MODIS, as discussed above. ASTER itself was not designed to measure atmospheric characteristics. Essentially, MODIS atmospheric water vapor and temperature profiles are combined with surface elevations



derived from a global digital elevation map, used to characterize concentrations of well-mixed gases, such as  $\text{CO}_2$ , and the ensemble is used to drive the MODTRAN3 atmospheric model to predict  $\tau$ ,  $S_{\uparrow}$  and  $S_{\downarrow}$  for the five ASTER bands. The MODIS temperature profiles may be accurate within 1.9 K and the total column water within 10% [6]. A 20% uncertainty in total column water corresponds to uncertainties in the ASTER land-leaving radiances ( $L'$ ) of 4.4% (band 10) or  $\leq 2.3\%$  (bands 11–14), and the atmospheric temperature uncertainty leads to errors in  $L'$  of a little less [5]. Because the atmospheric errors are highly correlated from band to band, the impact on TES is smaller than might be imagined; the chief effect is to change MMD by  $\sim 2\%$ , equivalent to an error of 0.004 emissivity units in  $\varepsilon_{\min}$  if MMD = 0.3, decreasing to zero for graybodies. The error at MMD = 0.3 corresponds to about 0.2 K. Atmospheric uncertainties that are uncorrelated from band to band, however, will have a larger effect on MMD, and this time the effect is larger for graybodies; for example, if the uncorrelated part is as large as 0.01 emissivity units, the error in  $\varepsilon_{\min}$  for graybodies is 0.019, dropping to  $\sim 0.007$  for MMD = 0.3.

The anticipated errors are roughly equivalent to 1 K or so in the ASTER temperature product—about the same amount attributable to scatter in the  $\varepsilon_{\min}$  versus MMD regression. This rough equivalence, however, presumes that the low-resolution (5-km) MODIS atmospheric profiles are actually representative of the local atmosphere at the 90-m ASTER scale. To the extent that this is not the case, errors in the atmospheric characterization may be the dominant source of uncertainty in the ASTER temperature and emissivity products.

#### E. Performance in the Presence of Uncompensated Atmospheric Effects

If atmospheric correction is inaccurate, the residual effects can degrade the performance of TES. ASTER band 10 is more affected by atmospheric absorption and emission than the other ASTER bands, by about a factor of two, because it is located closest to the edge of the TIR atmospheric window. Numerical simulation suggests that, under these conditions, TES performance may be improved by eliminating ASTER band 10 and running TES on ASTER bands 11–14. This necessitates using different  $\varepsilon_{\min}$ -MMD regression coefficients and different test values and constants throughout the algorithm. Alternative regressions for different subsets of bands have been calculated and are included in the TES code, but they are not reported here. For ASTER bands 11–14, the scatter about the regression line is nearly identical to the scatter for the five-band case, such that little precision is lost by dropping band 10. Once the TES  $T$  has been found from the subset of bands, it is used to calculate the emissivity spectrum for all five bands, including ASTER band 10. As TES is currently implemented, the four-band option (ASTER bands 11–14) can be invoked by user control if band 10 results are found by the user to be flawed. There is no code in place to recognize this condition automatically, except in the case for which the QA data from the  $L'$  product indicate that band 10 data were not acquired or lost in transmission to earth. For most other band subsets,

the performance is degraded due to excessive scatter about the regression line.

### V. PERFORMANCE OF TES

TES processes an ASTER image ( $\sim 650 \times 650$  pixels) in 4.8–6.0 min on a DEC Alpha-3000/900 computer running at 275 MHz. We have tested the reliability of the TES products by 1) numerical simulation and 2) processing six calibrated, atmospherically corrected TIMS images for which field data were available. In the first approach, radiances estimated from library spectra using Planck's Law are passed through TES. These results give the most insight into the workings of the TES algorithm itself. The TIMS images may provide a more realistic test, but their preparation naturally involves the opportunity for error unrelated to TES. Difficulties encountered have included minor shifts in TIMS band wavelengths, requiring periodic recalibration, high-frequency temperature fluctuations in the onboard blackbodies due to turbulent flow of air across the instrument bay, necessitating construction of air dams, and sensing of the fuselage bay walls at high scan angles. These effects are all correctable in principle.

#### A. Numerical Simulation Results

Overall, the TES algorithm operating on error-free input radiances can recover temperatures for a wide range of surfaces within  $\sim 1.5$  K of the correct value and emissivities within  $\sim 0.015$ . For numerically simulated radiance emitted from surfaces at 300 K, based on the field emissivity spectra in our library, 95% (two standard deviations) of the recovered temperatures were within 1.5 K and 68% (one standard deviation) were within 0.3 K, for example. In comparison, NEM temperatures recovered by simply assuming that the emissivity for a given band has its average library value of 0.97 are accurate to  $\pm 1.7$  K. However, TES uncertainties are far less sensitive to ground temperature than NEM uncertainties are. This is a crucial advantage in areas of rugged relief because sun-facing (warm) and shadowed (cool) hillslopes will appear the same. If the ground temperature of vegetation is hypothetically increased from 240 to 340 K, the accuracy of TES  $T$  changes from  $-0.6$  to  $-1.0$  K, whereas the accuracy of NEM  $T$  changes from  $-1.0$  to  $-2.0$  K.

A second advantage of TES is its decreased sensitivity to  $\varepsilon_{\max}$ , compared to the NEM algorithm, for which  $T$  is simply proportional to the assumed value. If  $\varepsilon_{\max}$  is varied over 0.94–1.00, NEM  $T$  values will vary by  $\sim 4$  K, and NEM  $\varepsilon$  spectra will change amplitude by  $\sim 0.06$ . In contrast, TES  $T$  and  $\varepsilon$  values will vary by only  $\sim 0.5$  K and  $< 0.01$ . This decreased sensitivity to assumptions, and the iterative correction for reflected sky irradiance, is the major strength of the TES approach.

TES performance is not related to scene composition in general, but to the scatter about the  $\varepsilon_{\min}$ -MMD regression line, scatter that is largely independent of MMD (Fig. 4). Monte Carlo simulation shows that the scatter of recovered temperatures due to measurement error ( $NE\Delta T$ ) is about the same as that due to the inherent scatter about this regression

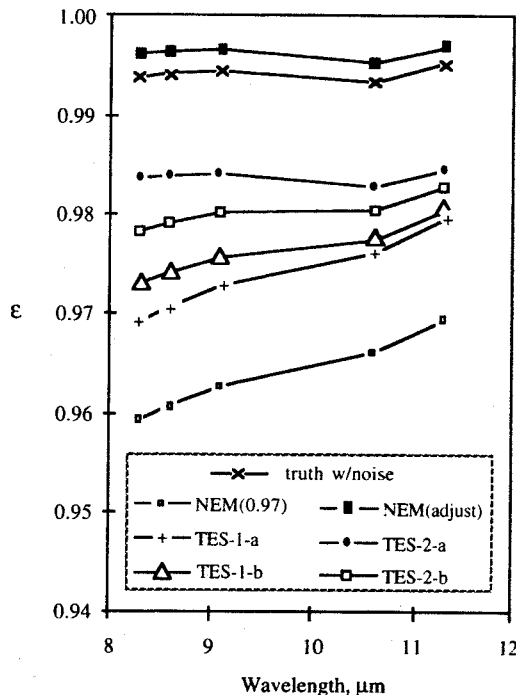


Fig. 5. Impact of  $S_1$  on apparent emissivities. The effect is greater for lower emissivities, even after accurate correction. Shown above: TES emissivity spectra for quartzite at 245, 248, and 343 K (effective sky temperature = 243 K).

line. Therefore, reducing  $NE\Delta T$  further will have little effect on TES results.

Although simple in concept, TES is a complex algorithm that performs differently for different surface compositions, surface temperatures, and atmospheric conditions. Comparisons to the NEM performance (above) are one way of indicating TES' capabilities in a general way. It is also helpful to examine the processing of a single radiance spectrum, in this case, a graybody (Fig. 5) similar to vegetation. For this example, a Monte Carlo experiment was run 30 times, such that the "measured" radiances are affected by different amounts of measurement "noise." The "truth" spectrum has an emissivity of about 0.995; the NEM emissivities, calculated erroneously assuming that  $\epsilon_{\max} = 0.97$ , average about 0.965, an error of about 0.03. In this instance, TES was started using this assumption, so this spectrum is also the starting point for TES. The successively higher, less-erroneous curves labeled TES-1(a) and (b) show spectra at intermediate processing stages, together reducing the error to 0.02. The next step was refining  $\epsilon_{\max}$  and recalculating a new NEM spectrum, which slightly overestimates the "correct" emissivities. A final pass (TES 2) through the remainder of the TES algorithm actually overcorrects, ending with an error of about 0.01. In this instance, the recalculated NEM curve provides the best approximation to the "truth," but this is not generally so because of the sensitivity of the NEM to  $\epsilon_{\max}$ . As described above, the initial assumed value for  $\epsilon_{\max}$  would be 0.99 instead of 0.97, but this example illustrates the capability for TES to iteratively improve its results and gives a sense of the magnitude of changes that are possible.

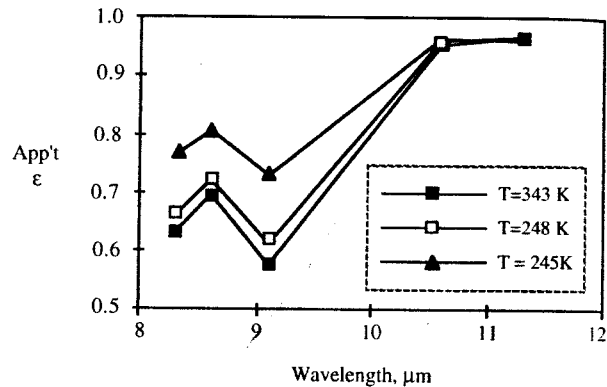


Fig. 6. Changes in apparent emissivity during execution of successive steps in TES. The plot shows the mean of 30 apparent emissivity spectra calculated for a graybody measured with ASTER  $NE\Delta T$  (Monte Carlo experiment). "Truth" is calculated correctly assuming  $T = 300$  K. The lowest curve is the NEM spectrum assuming  $\epsilon_{\max} = 0.97$ . The next two higher curves (TES-1 a, b) show the improvement obtained by the first pass through TES: for a, the apparent MMD was used, but for b the corrected value was (minimizing  $r$ ). The top curve (filled squares) is the recalculated NEM spectrum obtained by refining  $\epsilon_{\max}$ . The remaining curves (TES-2 a, b) are TES spectra based on the recalculated NEM temperature.

Fig. 6 illustrates the magnitude of the compensation for sky irradiance on a spectrum of quartzite for a cold sky approximated by a 243 K blackbody. Three quartzite temperatures are indicated: 245, 248, and 343 K, illuminated by the 243 K sky. The third case corresponds roughly to a sunlit desert soil, and it is essentially unaffected by reflected sky irradiance: the colder surfaces are affected more. Even for a wide range of surface temperatures, emissivity adjustment is on the order of 0.05 or less, even for deep reststrahlen features.

The numerical simulations assure us that, in general, TES outperforms NEM and the other TES algorithms. The major sources of uncertainty are the regression, the atmospheric correction, and measurement error. These are all independent of each other and all roughly the same size. In general, the compound errors are probably close to  $\pm 1.5$  K and 0.015 emissivity units. Numerical simulation results are discussed at greater length by Gillespie *et al.* [24].

### B. Tests on Simulated ASTER Images

Three ASTER images (Fig. 7) were simulated from calibrated TIMS overflights in clear air of Castaic Lake and Lake Tahoe, both in California, and of the south coast of Hawaii [42]. These images are used to test  $T$  and  $\epsilon$  recovery over water targets (low MMD). Three additional images have been prepared over a single geologic target, the playa in Railroad Valley and test recovery over land areas having high MMD (Figs. 8 and 9). TIMS has similar  $NE\Delta T$  and spectral bands to ASTER. Radiosonde atmospheric probes and Reagan Sun Photometer measurements of total water vapor, together with LOWTRAN 7 and MODTRAN2 and 3 atmospheric models [8]–[10], [43], were used to estimate  $\tau$ ,  $S_1$  and  $S_2$  at the time of overflight [44]. In addition,  $S_1$  was measured by the Jet Propulsion Laboratory's  $\mu$ FTIR spectrometers, using gold and bronze reflectance standards. These data were used to correct field spectra for reflected skylight. Surface radiant

Fig. 7. TI  
000 m  
400 H  
Water  
Tahoe  
made.

temperat  
temperat  
temperat  
and atm  
MS ov  
The C  
then  
]. For  
ures av  
emi  
9.0  $\pm$   
m. TES  
respon  
mosph  
the R  
The Li  
ountain  
Fig. 7  
low ter  
spectiv  
1.0  $\pm$   
sumin  
TES  $T$ 's  
uncertai  
TES  $\epsilon$  s  
lake.

The H  
can ne  
water  
steam  
can ter  
296 K  
temperat  
three d  
the c  
spectiv  
and othe  
discrepa  
Railro  
(1995–1  
ponds s  
Fig. 8(a)  
respectiv  
version

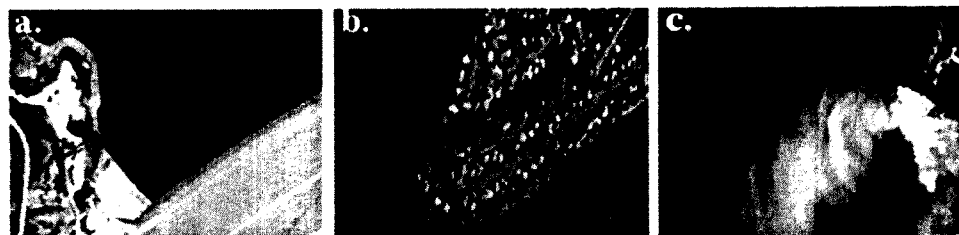


Fig. 7. TES temperature images from simulated ASTER images acquired by airborne TIMS, with  $NE\Delta T = 0.2^\circ\text{K}$  [1], over (a) Castaic Lake, CA ( $\sim 900$  m amsl;  $\sim 1130$  PST, 9 March 1994), (b) Lake Tahoe, CA ( $\sim 2000$  m amsl;  $\sim 1030$  PDT, 23 May 1995), and (c) the south coast of Hawaii ( $\sim 0400$  HST, 1 October 1988). Subscene size:  $100 \times 200$  pixels. Resolution is  $\sim 5.5\text{--}7.5$  m/pixel; subscenes are about 1.2 km across; north is to the top. Water temperatures were measured from buoys and Radiosonde atmospheric profiles were made, all at the time of overflight for Castaic Lake and Lake Tahoe. Radiometric temperatures were measured for the ocean near the lava entry point in the Hawaii image, but only three days before the image was made. Radiosonde data at the time of overflight were available from Hilo.

temperatures were measured with calibrated, insulated, and temperature-controlled Everest radiometers ( $\pm 0.5$  K); water temperatures were measured with buoys. Field temperature and atmospheric data were measured concurrently with the TIMS overflights, except as noted.

The Castaic Lake image [Fig. 7(a)] is of a reservoir, the earthen dam that impounds it, and sparsely vegetated hills [44]. Forty-nine buoy measurements of lake surface temperatures averaged  $287.9 \pm 0.3$  K. TIMS radiances, with correct emissivities specified, indicate a water temperature of  $289.0 \pm 1.6$  K, suggesting inaccurate atmospheric compensation. TES  $T$  was  $\sim 290.6$  K, and the average emissivities were correspondingly low (by  $\sim 0.05$ ). We attribute the inaccurate atmospheric compensation to incorrectly calibrated hygrometers in the Radiosondes, a problem that was corrected in 1997.

The Lake Tahoe image includes the lake and forested, snowy mountains, in addition to Dollar Point, a subdivision shown in Fig. 7(b). Field measurements of water, air, and melting snow temperatures were  $\sim 280.3$ ,  $\sim 283.1$ , and  $\sim 273.1$  K, respectively. TES  $T$  values of water, forest and snow were  $281.0 \pm 0.4$ ,  $283.9 \pm 0.6$ , and  $273.7 \pm 0.4$  K, respectively. Assuming forest and air temperatures were the same, the mean TES  $T$ 's were systematically  $0.6\text{--}0.8$  K too high, but within the uncertainty predicted from the numerical simulation studies. TES  $\epsilon$  spectra for Lake Tahoe were consistent with Castaic Lake.

The Hawaii image shows an active lava flow entering the ocean near Kapa'ehu, accounting for the plume-like patterns in the water and for the wide range of temperatures there. A cloud of steam drifts west (left) from the entry point. Radiometric ocean temperatures measured three days before overflight were  $\sim 296$  K, rising to  $\sim 330$  K near the lava [44]. TES  $T$  ocean temperatures were  $305 \pm 0.6$  K,  $\sim 9$  K higher than the earlier (three days) radiometric temperatures. Emissivities recovered for the ocean were too low by  $0.05\text{--}0.02$  (bands 10 and 12, respectively). Uncorrected absorption and emission by  $\text{SO}_2$  and other gases from the lava may account for some of the discrepancies.

Railroad Valley images for three successive years (1995–1997) were analyzed. Fig. 8 shows the playa, shallow ponds surrounded with reeds, and alluvial fans in 1996. Fig. 8(a)–(c) show radiance, TES  $T$ , and TES  $\epsilon$  images, respectively; Fig. 8(d) is a decorrelation-stretched false-color version of the same scene, indicating clearly the spectral

homogeneity of the playa validation site (A). Results from 1995 to 1996 were consistent with those from California and Hawaii. Running TES without band 10 cut pond temperature discrepancies in half, indicating inaccurate atmospheric water profiles. After correcting the Radiosonde hygrometer calibration in 1997, TES emissivities for the pond and playa sites were brought into agreement with laboratory and field measurements (Fig. 9). Precisions for  $\epsilon$  for homogeneous areas on the images were  $\leq 0.006$ . We attribute some of the rms "error" of 0.018 for the playa to difficulties in comparing spectra made at different scales (6.4 m versus 10 cm). TES pond temperatures were  $290.8 \pm 0.4$  K, 1.7 K less than the buoy temperatures. Because of evaporation, water skin temperatures may be as much as 4 K lower than buoy temperatures. TES temperatures of  $314.2 \pm 0.3$  K (6/1/96) for playa site A were indistinguishable from the field temperatures,  $314.3 \pm 0.9$  K, measured with the Everest radiometers during overflight and assuming that  $\epsilon = 0.93$ .

Correcting for sky irradiance in the TES algorithm reduced apparent water temperatures by  $\sim 0.2$  K for the California and Nevada sites and  $\sim 0.5$  K for Hawaii.

## VI. DISCUSSION AND CONCLUSIONS

TES is designed to minimize systematic errors in temperature and emissivity and to limit errors in the tilt and shape of recovered emissivity spectra. This is accomplished largely through compensation for reflected sky irradiance and recourse to an empirical relationship between emissivity contrast and amplitude to eliminate the indeterminacy of the inversion problem. This constraint turns out to be better than the assumptions used in other algorithms we inspected; in particular, it is an improvement over the assumption (that  $\epsilon_{\text{max}}$  is known) in the NEM approach and Wien's approximation in the ADE approach. The NEM and ADE algorithms are hybridized to form the basis for TES. The biggest difference between TES and NEM performance is in the reduced sensitivity of TES to scene temperature, especially in the emissivity product, and the shape, especially the tilt, of the TES emissivity spectra is more faithful than the ADE spectra. Because TES compensates for reflected sky irradiance, TES emissivity spectra have higher contrast than NEM or ADE spectra.

Numerical simulations and field validation studies with TIMS aircraft data suggest that TES performs within its



Fig. 8. TES results from simulated ASTER data acquired by TIMS over Railroad Valley, NV, playa (1435 m amsl)  $\sim$ 1100 PDT, 1 June 1996. Resolution is 15 m/pixel: (a) TIMS Radiance data, simulated ASTER band 13 ( $10.6 \mu\text{m}$ ), showing test areas for which field temperatures and laboratory reflectance spectra were measured: A is the playa center; B and C are shore; D is the yardangs; and E is the ponds. (b) Temperature image recovered by TES. (c) Emissivity image, ASTER band 12, recovered by TES. (d) False-color decorrelation-stretched image made from ASTER bands 10 = B, 12 = G, and 13 = R. Decorrelation stretching subdues correlated radiance variations due to scene temperatures and exaggerates spectral differences.

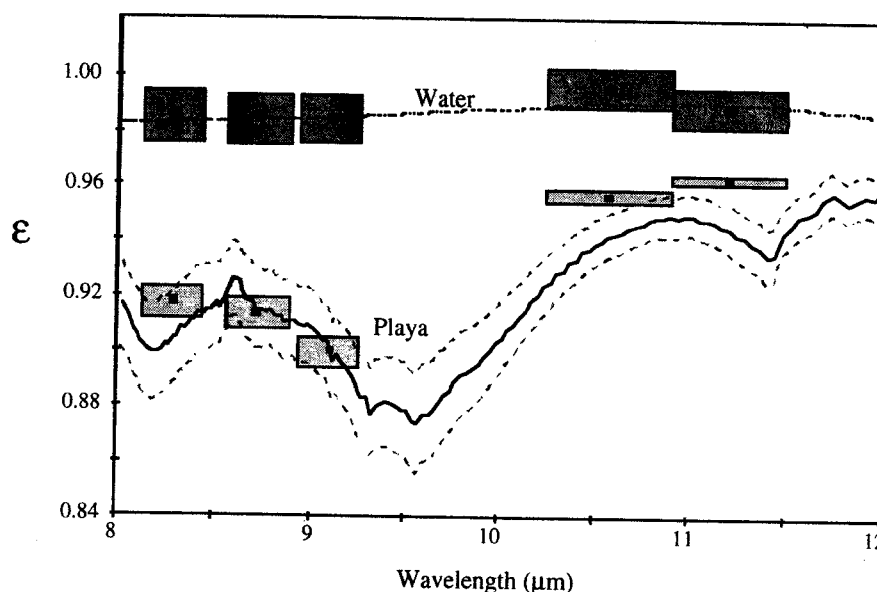


Fig. 9. TES emissivity pseudospectra (1000 PDT, 23 June 1997) compared to emissivity spectra, Railroad Valley playa. Water spectrum: average value from [45]. Playa spectrum: average  $\pm 1$  standard deviation for 99 field emissivity spectra of playa, Site A. Darker solid bars: TES  $\epsilon$  values for ponds, Site E. Lighter bars: TES  $\epsilon$  values for playa, Site A. Height of the bars indicates  $\pm 1$  standard deviation; width indicates the half-amplitude ASTER bandwidths. Water temperatures were measured with buoys, playa temperatures were measured with Everest radiometers, and Radiosonde profiles were measured, all at the time of overflight. Emissivity spectra were measured in the field the day of overflight, and samples were collected the day before overflight for later measurement in the laboratory. Total column water at the time of overflight was  $0.39 \text{ g/cm}^2$ , rising to  $0.71 \text{ g/cm}^2$  2 h later.

design specifications to recover temperatures and emissivities within 1.5 K and 0.015. In all four experiments for which concurrent Radiosonde water-vapor profiles were suspect, the emissivity inaccuracies were worst in ASTER band 10, the band most influenced by atmospheric effects. Deleting band 10 while running TES improved agreement with field temperature measurements, suggesting that this strategy may be of general use when atmospheric compensation is uncertain. This modification is without substantial statistical effect on

the output precisions, unless the maximum emissivity occurs in band 10 because the different  $\epsilon_{\text{min}}$ -MMD regression has similar scatter to the five-band case.

Scatter about the  $\epsilon_{\text{min}}$ -MMD regression line appears to be a property of natural surfaces and not experimental artifact. It is a fundamental feature of TES that limits its performance. For high MMD scenes, the scatter is coincidentally and roughly equivalent to the ASTER  $NE\Delta T$  of 0.3 K and to engineering predictions of  $\sim 1$  K radiometric accuracy. Errors due to scatter

about the  
as v  
from n  
the fir  
ing  $\epsilon$ ,  
improv  
ulate  
However,  
accuracy  
algorithm  
is not.  
-MM  
uncertain  
Atmosp  
TES perf  
for many  
atmosphe  
tion fo  
the AS  
ed on  
equiv  
or thi  
oughly  
ement  
ertain  
ough  
to atr  
imple  
or ma  
of mir  
ounted  
ospher  
ected s  
for lim  
orts T  
er deg  
Most s  
tain n  
els. Th  
rest. N  
ression  
error ir  
gh sur  
line.  
these  
tributi  
ral su  
may  
on a v  
probably r  
imulation  
number o  
run, for  
by ASTE  
for two t  
the other  
scatter abo  
asymptoti

about the regression line are most serious for graybodies, such as vegetation and water. For these important scene types, random measurement errors affecting MMD can be amplified in the final  $T$  and  $\varepsilon$  products, leading us to treat them by forcing  $\varepsilon_{\min}$  to a specified value to minimize the effect on  $T$ .

Improvements in ASTER sensitivity and noise levels would translate into improved TES precision for natural graybodies. However, even for  $NE\Delta T = 0$ , TES could not match the accuracy of dedicated split-window sea-surface temperature algorithms because these presume that  $\varepsilon$  is known and TES does not. For geologic surfaces, the inherent variability on the  $\varepsilon_{\min}$ -MMD plane, not the  $NE\Delta T$ , is the greater source of uncertainty.

Atmospheric compensation may be the effective limit on TES performance with ASTER data during the EOS mission. For many, perhaps most scenes, the critical parameters are atmospheric transmissivity and path radiance. Errors in correction for these parameters propagate directly into  $T$  and  $\varepsilon$ . The ASTER TIR atmospheric compensation algorithm [5], based on MODIS atmospheric profiles, introduces uncertainties equivalent to radiometric errors of a few percent. For dry or thin atmospheres, the contribution to TES uncertainty is roughly the same as that due to the regression and measurement error, probably less than 2 K; for humid air, the uncertainty may be greater. It is worth emphasizing that, although not an attribute of the TES algorithm itself, errors due to atmospheric compensation will be a major concern in any implementation of the algorithm.

For many scenes, sky irradiance reflected from the scene is of minor significance; for example, at Castaic Lake, it accounted for only 0.2 K. For humid atmospheres or warm atmospheres over cold scenes, however, the correction for reflected sky irradiance may be larger, even the most important factor limiting TES performance. Uncorrected sky irradiance distorts TES emissivity spectra, but affects temperatures to a lesser degree.

Most soil or rock surfaces, and open-canopy vegetation, contain multiple components at the 90-m scale of ASTER pixels. Therefore, performance of TES for mixed pixels is of interest. Mixtures of scene materials fall near the  $\varepsilon_{\min}$ -MMD regression line if the endmembers do also. Potential sources of error include a mixture of blackbody cavity radiation from rough surfaces, since ideal blackbodies fall above the regression line. Theoretical studies with radiosity models suggest that these effects will be minor because multiple-scattering contributions rarely exceed ~20% of the total radiance from natural surfaces.

It may be useful to apply TES to multispectral TIR images from a variety of imaging systems. To be effective, TES probably requires at least three or four bands of data; numerical simulations show that uncertainties become larger as the number of bands is reduced further. It is possible for TES to run, for example, on only four of the five bands acquired by ASTER, with little degradation in performance, whereas for two bands, the products are only half as precise. On the other hand, as the number of bands is increased, the scatter about the  $\varepsilon_{\min}$ -MMD regression line is reduced until it asymptotically approaches a limit of about 40% of the scatter

for the ASTER case. This limit is effectively reached with 30 bands of TIR data (8–12  $\mu\text{m}$ ). From this viewpoint, there is little motivation to reduce  $NE\Delta T$  below about 0.1 K, since performance is limited to about  $\pm 0.3$  K (one standard deviation) by the regression anyway. The chief benefit of "noiseless" data would be to improve TES performance over vegetation, snow, and water. This is a significant improvement, if only because much of the land surface is heavily vegetated. However, it is safe to conclude that major improvements in atmospheric characterization must accompany improved sensors if those improvements are to be translated into more reliable temperature and emissivity data.

TES requires further testing on calibrated, atmospherically corrected TIR data before routine use by the remote-sensing community. However, we conclude that TES is a useful and general algorithm for recovering land-surface temperature and emissivities from multispectral TIR imaging systems. The fundamental limitations are the variability in the  $\varepsilon_{\min}$ -MMD relationship for natural surfaces and atmospheric characterization and correction. Future refinements of TES may be possible, but performance characteristics reported in this discussion are probably close to their ultimate limits for ASTER. Even with ideal noiseless, hyperspectral instruments, together with perfect atmospheric compensation, uncertainties can only be reduced by a factor of two or three with the TES approach.

#### ACKNOWLEDGMENT

The authors would like to thank their colleagues on ASTER's Temperature/Emissivity Working Group for helpful advice and criticism and especially J. Salisbury for providing spectra. They also would like to thank E. Abbott, F. Palluconi, W. Li, D. Gu, and D. Sabol for their tireless help as well as P. Christensen and two anonymous reviewers for their careful critiques that greatly improved the quality and readability of the manuscript.

#### REFERENCES

- [1] F. Palluconi and G. R. Meeks, "Thermal infrared multispectral scanner (TIMS): An investigator's guide to TIMS data," Jet Propul. Lab., Pasadena, CA, JPL Publ. 85-32, 1985.
- [2] A. B. Kahle, F. Palluconi, S. Hook, V. J. Realmuto, and G. Bothwell, "The Advanced Spaceborne Thermal Emission and Reflectance Radiometer (ASTER)," *Int. J. Imaging Syst. Tech.* 3, pp. 144–156, 1991.
- [3] Y. Yamaguchi, H. Tsu, and H. Fujisada, "A scientific basis of ASTER instrument design," in *Proc. SPIE*, 1993, pp. 150–160.
- [4] H. Fujisada and A. Ono, "Anticipated performance of ASTER instrument in EM design phase," *Proc. SPIE*, 1993, pp. 187–197.
- [5] F. Palluconi, G. Hoover, R. Alley, M. Jentoft-Nilsen, and T. Thompson, "An atmospheric correction method for ASTER Thermal radiometry over land, revision 2: ASTER standard data product AST09, Level 2 Radiance—TIR, land-leaving," Jet Propul. Lab., Pasadena, CA, Aug. 16, 1996. <http://asterweb.jpl.nasa.gov/asterhome/atbd/ATBD-AST-04.doc>.
- [6] W. P. Menzel and L. E. Gumley, "MODIS atmospheric profile retrieval algorithm theoretical basis document, version 3," Univ. Wisconsin-Madison, Madison WI, Sept. 3, 1996, p. 30, <http://ftpwww.gsfc.nasa.gov/MODIS/MODIS.html/atbd-mod11.pdf/mod.07.pdf>.
- [7] C. Prabhakara and G. Dalu, "Remote sensing of surface emissivity at 9  $\mu\text{m}$  over the globe," *J. Geophys. Res.*, vol. 81, no. 21, pp. 3719–3724, 1976.
- [8] L. W. Abreu, F. X. Kneizys, G. P. Anderson, J. H. Chetwynd, A. Berk, L. S. Bernstein, and D. C. Robertson, "MODTRAN," in *Proc. 1991 Remote Sensing Conf.*, El Paso, TX, 1991.

- [9] G. P. Anderson, J. H. Chetwynd, J.-M. Theriault, P. Acharya, A. Berk, D. C. Robertson, F. X. Kniezys, M. L. Hoke, L. W. Abreu, and E. P. Shettle, "MODTRAN2: Suitability for remote sensing," in *Workshop Atmos. Correction Landsat Imagery*, P. N. Slater and L. D. Mendenhall, Eds. Torrance, CA: Geodynamics, 1993.
  - [10] F. X. Kniezys, L. W. Abreu, G. P. Anderson, J. H. Chetwynd, E. P. Shettle, A. Berk, L. S. Bernstein, D. C. Robertson, P. Acharya, L. S. Rothman, J. E. A. Selby, W. O. Gallery, and S. A. Clough, "The MODTRAN 2/3 report and LOWTRAN 7 model," L. W. Abreu and G. P. Anderson, Eds., Phillips Lab., Geophys. Directorate, PL/GPOS, Hanscom AFB, MA 01731, Contract F19628-91-C-0132, Nov. 1, 1996.
  - [11] K. Masuda, T. Takashima, and Y. Takayama, "Emissivity of pure and sea waters for the model sea surface in the infrared window region," *Remote Sens. Environ.*, vol. 24, pp. 313-329, 1988.
  - [12] I. J. Barton, "Transmission model and ground truth investigation of satellite derived sea surface temperatures," *J. Clim. Appl. Meteorol.*, vol. 24, pp. 508-516, 1985.
  - [13] L. M. McMillan and D. S. Crosby, "Theory and validation of the multiple window sea surface temperature technique," *J. Geophys. Res.*, vol. 89, no. C3, pp. 655-666, 1984.
  - [14] C. Prabhakara, G. Dalu, and V. G. Kunde, "Estimation of sea surface temperature from remote sensing in the 11- to 13- $\mu$ m window region," *J. Geophys. Res.*, vol. 79, no. 33, pp. 5039-5044, 1974.
  - [15] O. B. Brown, "MODIS Infrared sea surface temperature algorithm," Algorithm Theoretical Basis Document, NASA Contract NAS5-31361, Oct. 21, 1996, <http://ftpwww.gsfc.nasa.gov/MODIS/MODIS.html/atbd-mod11.pdf>.
  - [16] Z. Wan and J. Dozier, "A generalized split-window algorithm for retrieving land-surface temperature from space," *IEEE Trans. Geosci. Remote Sensing*, vol. 34, pp. 892-905, July 1996.
  - [17] J. C. Price, "Land surface temperature measurements from the split window bands of the NOAA 7 advanced very high resolution radiometer," *J. Geophys. Res.*, vol. 89, pp. 7231-7237, 1984.
  - [18] F. Becker, "The impact of spectral emissivity on the measurement of land surface temperatures from a satellite," *Int. J. Remote Sensing*, vol. 8, no. 10, pp. 1509-1522, 1987.
  - [19] A. Vidal, "Atmospheric and emissivity correction of land surface temperatures measured from satellite using ground measurements or satellite data," *Int. J. Remote Sensing*, vol. 12, no. 12, pp. 2449-2460, 1991.
  - [20] Z. Wan and J. Dozier, "Land-surface temperature measurement from space: Physical principles and inverse modeling," *Trans. Geosci. Remote Sensing*, vol. 27, no. 3, pp. 268-278, Jan. 1989.
  - [21] A. B. Kahle, D. P. Madura, and J. M. Soha, "Middle infrared multispectral aircraft scanner data analysis for geological applications," *Appl. Opt.*, vol. 19, pp. 2279-2290, 1980.
  - [22] M. J. Abrams, E. A. Abbott, and A. B. Kahle, "Combined use of visible, reflected infrared and thermal infrared images for mapping Hawaiian lava flows," *J. Geophys. Res.*, vol. 96, no. B1, pp. 475-484, 1991.
  - [23] A. Gillespie, "Spectral mixture analysis of multispectral thermal infrared images," *Rem. Sens. Environ.*, vol. 42, pp. 137-145, 1992.
  - [24] A. Gillespie, S. Rokugawa, S. J. Hook, T. Matsunaga, and A. B. Kahle, "Temperature/emissivity separation algorithm theoretical basis document, version 2.3," Jet Propulsion Laboratory, Pasadena, CA, Aug. 16, 1996, <http://asterweb.jpl.nasa.gov/asterhome/atbd/ATBD-AST-03.doc>.
  - [25] F. Becker and Z. L. Li, "Temperature-independent spectral indices in thermal infrared bands," *Rem. Sens. Environ.*, vol. 32, p. 17-33, 1990.
  - [26] S. J. Hook, A. R. Gabell, A. A. Green, and P. S. Kealy, "A comparison of techniques for extracting emissivity information from thermal infrared data for geologic studies," *Rem. Sens. Environ.*, vol. 42, pp. 123-135, 1992.
  - [27] K. Watson, "Spectral ratio method for measuring emissivity," *Rem. Sens. Environ.*, vol. 42, pp. 113-116, 1992.
  - [28] K. Watson, F. A. Kruse, and S. Hummer-Miller, "Thermal infrared exploration in the Carlin trend, northern Nevada," *Geophys.*, vol. 55, no. 1, pp. 70-79, 1990.
  - [29] K. Watson, "Two-temperature method for measuring emissivity," *Rem. Sens. Environ.*, vol. 42, pp. 117-121, 1992.
  - [30] R. J. P. Lyon, "Analysis of rocks by spectral infrared emission (8 to 25 microns)," *Econ. Geol.*, vol. 60, pp. 715-736, 1965.
  - [31] A. Gillespie, "Lithologic mapping of silicate rocks using TIMS," in *TIMS Data Users' Workshop*. Pasadena, CA: Jet Propul. Lab., JPL Publication 86-38, 1995, pp. 29-44.
  - [32] V. J. Realmuto, "Separating the effects of temperature and emissivity: Emissivity spectrum normalization," in *Proc. 2nd TIMS Workshop*. Pasadena, CA: Jet Propul. Lab., JPL Publication 90-55, 1990.
  - [33] P. S. Kealy and A. R. Gabell, "Estimation of emissivity and temperature using alpha coefficients," in *Proc. 2nd TIMS Workshop*. Pasadena, CA: Jet Propul. Lab., JPL Publication 90-55, 1990.
  - [34] P. S. Kealy and S. Hook, "Separating temperature and emissivity in thermal infrared multispectral scanner data: Implication for recovering land surface temperatures," *Trans. Geosci. Remote Sensing*, vol. 31, pp. 1155-1164, Nov. 1993.
  - [35] T. Matsunaga, "A temperature-emissivity separation method using an empirical relationship between the mean, the maximum, and the minimum of the thermal infrared emissivity spectrum," *J. Rem. Sens. Soc. Japan*, vol. 14, no. 2, pp. 230-241, 1994 (in Japanese with English abstract).
  - [36] Z. Wan and W. Snyder, "MODIS land-surface temperature algorithm theoretical basis document (LST ATBD), version 3.2," Contract NAS5-31370, p. 73, Dec. 1996, <http://ftpwww.gsfc.nasa.gov/MODIS/MODIS.html/atbd-mod25.pdf>.
  - [37] Z. Wan and Z. L. Li, "A physics-based algorithm for retrieving land-surface emissivity and temperature from EOS/MODIS data," *IEEE Trans. Geosci. Remote Sensing*, vol. 35, pp. 980-996, July 1997.
  - [38] T. Schmugge, S. Hook, and A. B. Kahle, "TIMS observations of surface emissivity in Hapex-Sahel," *Proc. IEEE Quant. Rem. Sens. Sci. Appl. Firenze, Italy*, 1995, vol. III, pp. 2224-2226.
  - [39] S. Hook and A. B. Kahle, "The JPL field emissivity spectrometer," in *Proc. 5th Airborne Visible/Infrared Imaging Spectrometer (AVIRIS) Workshop*. Pasadena, CA: Jet Propul. Lab., JPL Pub. 90-54, 1995, pp. 17-18.
  - [40] J. W. Salisbury, L. S. Walter, and D. M. D'Aría, "Mid-infrared (2.5-13.5  $\mu$ m) spectra of igneous rocks," U.S. Geological Survey Open-File Rep. 88-686, 1988, p. 132.
  - [41] ———, "Emissivity of terrestrial materials in the 8-14  $\mu$ m atmospheric window," *Remote Sens. Environ.*, vol. 42, pp. 83-106, 1992.
  - [42] V. J. Realmuto, K. Hon, A. B. Kahle, E. A. Abbott, and D. C. Pieri, "Multispectral thermal infrared mapping of the 1 Oct. 1988 Kupaiana flow field, Kilauea volcano, Hawaii," *Bull. Volcanol.*, vol. 55, pp. 33-44, 1992.
  - [43] F. X. Kniezys, E. P. Shettle, L. W. Abreu, J. H. Chetwynd, G. P. Anderson, W. O. Gallery, J. E. A. Selby, and S. A. Clough, "User guide to LOWTRAN 7," Air Force Geophys. Lab. Rep. AFGL-TR-88-0177, Hanscom AFB, MA, 1988.
  - [44] V. J. Realmuto, "Report of TIMS airborne calibration experiment: Castaic Lake, California, 9 Mar. 1994," Jet Propul. Lab., Pasadena, CA, May 10, 1994, p. 18.
  - [45] J. W. Salisbury, personal communication, 1995.
  - [46] H. Tonooka, personal communication, 1996.
  - [47] D. Gu, personal communication, 1998.
  - [48] T. Cudahy, personal communication, 1996.
- Alan Gillespie, photograph and biography not available at the time of publication.
- Shuichi Rokugawa, photograph and biography not available at the time of publication.
- Tsuneeo Matsunaga, photograph and biography not available at the time of publication.
- J. Steven Cothorn, photograph and biography not available at the time of publication.
- Simon Hook, photograph and biography not available at the time of publication.
- Anne B. Kahle, photograph and biography not available at the time of publication.

Bi  
DavAbstract-  
(GRES) is  
GRES objFor  
the E  
of ra  
analy  
data.  
Doub  
and t  
Provi  
fluxes  
Provi  
time  
surfa  
order  
ination  
an impmanuscript  
A. Wieli  
Kratz, R  
atmospheric  
33681-000  
L. Smith  
burg, V  
D. Cess  
NY 11  
CoaklA. H. Ci  
els, Belg  
Donner  
Geophys  
Kandel  
technique  
D. King  
USA.  
J. Miller  
National  
USA.  
Ramanat  
California,  
A. RandL. Stow  
National  
DC 20  
M. Welcl  
3307 USA.  
Publisher It